

Three-Dimensional Imaging of Metabolites in Tissues under Ambient Conditions by Laser Ablation Electrospray Ionization Mass Spectrometry

Peter Nemes, Alexis A. Barton, and Akos Vertes*

Department of Chemistry, W. M. Keck Institute for Proteomics Technology and Applications, George Washington University, Washington, DC 20052

Three-dimensional (3D) imaging of molecular distributions offers insight into the correlation between biochemical processes and the spatial organization of a biological tissue. Simultaneous identification of diverse molecules is a virtue of mass spectrometry (MS) that in combination with ambient ion sources enables the atmospheric pressure investigation of biomolecular distributions and processes. Here, we report on the development of an MS-based technique that allows 3D chemical imaging of tissues under ambient conditions without sample preparation. The method utilizes laser ablation electrospray ionization (LAESI) for direct molecular imaging with lateral and depth resolutions of $\sim 300\ \mu\text{m}$ and $30\text{--}40\ \mu\text{m}$, respectively. We demonstrate the feasibility of LAESI 3D imaging MS of metabolites in the leaf tissues of Peace lily (*Spathiphyllum lynnise*) and the variegated Zebra plant (*Aphelandra squarrosa*). Extensive tandem MS studies help with the structure identification of the metabolites. The 3D distributions are found to exhibit tissue-specific metabolite accumulation patterns that correlate with the biochemical roles of these chemical species in plant defense and photosynthesis. Spatial correlation coefficients between the intensity distributions of different ions help to identify colocalization of metabolites and potentially uncover connections between metabolic pathways.

Many of the current three-dimensional (3D) biomedical imaging methods achieve exquisite lateral and depth resolution for in vivo imaging by relying on the interaction of electromagnetic radiation or particles with the specimen.¹ For example, coherent anti-Stokes Raman scattering has demonstrated capabilities to follow lipid distributions on the cellular or subcellular level.² Several of these techniques, however, exhibit limited chemical selectivity, are specific to a small number of molecular species, and often require the introduction of fluorescent or other molecular labels. These restrictions are less prevalent in methods based on mass spectrometry (MS) that simultaneously report the

distributions for diverse molecular species without the need for fluorescent or other labels.^{3,4}

Established imaging MS methods, such as secondary ion mass spectrometry (SIMS) and matrix-assisted laser desorption ionization (MALDI), and recent developments including nanostructure initiator mass spectrometry have demonstrated exceptional capabilities in capturing the 2D and 3D distributions of endogenous and drug molecules in tissue and whole-body sections.^{5–10} Recently, using C_{60} primary ions, time-of-flight SIMS has enabled 3D studies of a freeze-dried oocyte and revealed the distribution of lipids and related molecules with excellent spatial resolution.⁴ Imaging vacuum MALDI MS, in combination with cryosectioning, can produce a series of 2D protein and peptide images that can be reconstructed in 3D.⁹ Characteristic to these methods, however, is the requirement for sample preparation and the need to perform the experiment in vacuum, preventing the study of live specimens.

Atmospheric pressure imaging MS circumvents these limitations by bringing the ionization step into the ambient environment while minimizing or eliminating treatment to the sample.¹¹ During the past few years, this field has experienced rapid development providing several ambient ion sources for imaging MS. For example, atmospheric pressure (AP) infrared MALDI^{12–14} has captured metabolite transport in plant vasculature,¹⁴ desorption

- (3) Northen, T. R.; Yanes, O.; Northen, M. T.; Marrinucci, D.; Uritboonthai, W.; Apon, J.; Golledge, S. L.; Nordstrom, A.; Siuzdak, G. *Nature* **2007**, *449*, 1033–U1033.
- (4) Fletcher, J. S.; Lockyer, N. P.; Vaidyanathan, S.; Vickerman, J. C. *Anal. Chem.* **2007**, *79*, 2199–2206.
- (5) Ostrowski, S. G.; Van Bell, C. T.; Winograd, N.; Ewing, A. G. *Science* **2004**, *305*, 71–73.
- (6) Khatib-Shahidi, S.; Andersson, M.; Herman, J. L.; Gillespie, T. A.; Caprioli, R. M. *Anal. Chem.* **2006**, *78*, 6448–6456.
- (7) McDonnell, L. A.; Heeren, R. M. A. *Mass Spectrom. Rev.* **2007**, *26*, 606–643.
- (8) Zhang, H.; Cha, S. W.; Yeung, E. S. *Anal. Chem.* **2007**, *79*, 6575–6584.
- (9) Andersson, M.; Groseclose, M. R.; Deutch, A. Y.; Caprioli, R. M. *Nat. Methods* **2008**, *5*, 101–108.
- (10) Yanes, O.; Woo, H.-K.; Northen, T. R.; Oppenheimer, S. R.; Shriver, L.; Apon, J.; Estrada, M. N.; Potchoiba, M. J.; Steenwyk, R.; Manchester, M.; Siuzdak, G. *Anal. Chem.* **2009**, *81*, 2969–2975.
- (11) Cooks, R. G.; Ouyang, Z.; Takats, Z.; Wiseman, J. M. *Science* **2006**, *311*, 1566–1570.
- (12) Laiko, V. V.; Taranenko, N. I.; Berkout, V. D.; Yakshin, M. A.; Prasad, C. R.; Lee, H. S.; Doroshenko, V. M. *J. Am. Soc. Mass Spectrom.* **2002**, *13*, 354–361.
- (13) Li, Y.; Shrestha, B.; Vertes, A. *Anal. Chem.* **2008**, *80*, 407–420.
- (14) Li, Y.; Shrestha, B.; Vertes, A. *Anal. Chem.* **2007**, *79*, 523–532.

* To whom correspondence should be addressed. E-mail: vertes@gwu.edu. Phone: 202-994-2717. Fax: 202-994-5873.

(1) Weissleder, R.; Pittet, M. J. *Nature* **2008**, *452*, 580–589.
(2) Evans, C. L.; Potma, E. O.; Puoris'haag, M.; Cote, D.; Lin, C. P.; Xie, X. S. *Proc. Natl. Acad. Sci. U.S.A.* **2005**, *102*, 16807–16812.

electrospray ionization (DESI)¹⁵ has imaged drugs of abuse in fingerprints¹⁶ and metabolite distributions in thin tissue sections,^{17–19} and laser ablation electrospray ionization (LAESI)^{20,21} has provided insight into metabolic differences between the sectors of variegated plants and described a simple form of depth profiling. Lateral imaging methods alone do not capture the localization of chemical species in the depth dimension.

Our previous paper discussed depth profiling at a particular position and lateral imaging separately.²¹ This raised the prospect of combining these two modes into 3D imaging. This proposition, however, has very important technical consequences regarding source stability, as it is much more challenging to maintain source stability for several hours required for the latter. There are also major differences in the potential amount and quality of information gathered. A 3D data set might exhibit correlations among metabolites and in relation to morphology that a simple depth profile does not capture. Improvements in ionization efficiency, signal stability, and depth resolution are required to provide reproducible quality depth profiling over at least 500 positions for the development of 3D molecular imaging with the LAESI ion source.

Here we report the first example of 3D imaging with MS under atmospheric pressure conditions that illuminates the relationship between tissue architecture and metabolism. In these experiments, LAESI 3D imaging MS is realized as a combination of lateral imaging and depth profiling by tissue ablation with single laser pulses of $\sim 2.94 \mu\text{m}$ wavelength. The O–H vibrations of the native water molecules in the tissue samples readily absorbed the laser pulse energy leading to ablation, i.e., the ejection of a microscopic volume of the sample in the form of neutral particulates and/or molecules.²² This plume was then intercepted by an electrospray, and the ablated material was efficiently postionized. Proof-of-principle experiments on leaves marked with ink confirmed that by gradually ablating through the tissue at every location, LAESI 3D imaging MS was able to recover the patterns on both the upper (adaxial) and the lower (abaxial) surfaces. Tandem MS was performed on numerous ions to help with structure assignments. The acquired 3D distributions of endogenous metabolites were interpreted in the context of metabolic pathways and their correlation with tissue morphology.

EXPERIMENTAL SECTION

Laser Ablation Electrospray Ionization Mass Spectrometry. The LAESI source was identical to the one we have recently described.^{20,21} The leaf tissues of peace lily (*Spathiphyllum lymise*) and zebra plant (*Aphelandra squarrosa*) were mounted on a three-axis translation stage, positioned 18 mm below the electrospray

axis. A Nd:YAG laser driven optical parametric oscillator (Vibrant IR, Oportek Inc., Carlsbad, CA) provided mid-infrared pulses at 2940 nm wavelength and 0.2 Hz repetition rate. This laser beam was used to ablate samples at 90° incidence angle, $\sim 3\text{--}5 \text{ mm}$ downstream from the tip of the spray emitter. During the *S. lymise* ($\sim 200 \mu\text{m}$ average leaf thickness) and *A. squarrosa* ($\sim 450 \mu\text{m}$ average leaf thickness) imaging experiments, the average output energy of a laser pulse was $0.1 \text{ mJ} \pm 15\%$ and $1.2 \text{ mJ} \pm 10\%$, which translated into a fluence of ~ 0.1 and $\sim 1.2 \text{ J/cm}^2$ at the focal point, respectively. Optical microscopy of the ablation marks in Z-stack mode confirmed that these single laser pulses removed $\sim 30\text{--}40 \mu\text{m}$ of the tissue (see the animated GIF image in the Supporting Information). The ablated material was intercepted by the electrospray plume, and the resulting ions were analyzed by an orthogonal acceleration time-of-flight mass spectrometer (Q-TOF Premier, Waters Co., Milford, MA) with a 1 s/spectrum integration time. The sampling cone of the mass spectrometer was located on axis with and 13 mm away from the tip of the spray emitter. The mass spectra were externally calibrated with sodium iodide clusters with a mass accuracy of $\sim 5 \text{ mDa}$ and a resolution of ~ 6000 (fwhm) between m/z 100 and 1000 in all experiments. Assignments of the detected ions to particular metabolites was facilitated by accurate mass measurements, comparisons of isotope distribution patterns, and tandem MS. Fragmentation was induced by collision-activated dissociation (CAD) in argon collision gas at 4×10^{-3} mbar pressure with the collision energy set between 15 and 30 eV.

Three-Dimensional Molecular Imaging with LAESI MS.

A three-axis translation stage was positioned with motorized actuators (LTA-HS, Newport Corp., Irvine, CA) to scan the sample surface on a 2D grid. The actuators had a travel range of 50 mm and a minimum incremental motion of $0.1 \mu\text{m}$. Thus, the ultimate resolution was determined by the focusing of the incident laser beam and the dimensions of the ablation craters ($\sim 300 \mu\text{m}$ in average diameter). At each lateral grid point, a depth profile was created with six laser pulses, while the generated ions were recorded with the mass spectrometer. Under these conditions, 3D imaging of a $12.5 \times 10.5 \times 0.45 \text{ mm}^3$ volume required a total analysis time of $\sim 5 \text{ h}$. Software was written in-house (LabView 8.0) to position the translation stage and render the analysis times to the corresponding X–Y–Z coordinates. The exported data sets of mass-selected ions were presented as layer-by-layer contour plot images with a scientific visualization package (Origin 7.0, OriginLab Co., Northampton, MA). Because the tissue composition was probed with $300 \mu\text{m}$ pixels at every $500 \mu\text{m}$ in the X and Y directions, $\sim 200 \mu\text{m}$ tissue areas were left intact during the imaging experiments (see Figure 1A). The image reconstruction algorithm applied in the current study interpolated the molecular composition over the intact areas.

Chemicals and Plants. Glacial acetic acid (TraceSelect grade) and gradient grade methanol and water were obtained from Sigma-Aldrich and used as received. The *S. lymise* and *A. squarrosa* plants were purchased from a local florist at an approximate age of one and a half years. The plants were watered every 2 days with $\sim 300 \text{ mL}$ of tap water to keep their soil moderately moist to the touch. No fertilizer was used during the experiments. Temperature and light conditions were $20\text{--}25 \text{ }^\circ\text{C}$ in light shade, protected from direct sun.

- (15) Takats, Z.; Wiseman, J. M.; Gologan, B.; Cooks, R. G. *Science* **2004**, *306*, 471–473.
- (16) Ifa, D. R.; Manicke, N. E.; Dill, A. L.; Cooks, G. *Science* **2008**, *321*, 805–805.
- (17) Wiseman, J. M.; Ifa, D. R.; Cooks, R. G.; Venter, A. *Nat. Protoc.* **2008**, *3*, 517–524.
- (18) Kertesz, V.; Van Berkel, G. J.; Vavrek, M.; Koeplinger, K. A.; Schneider, B. B.; Covey, T. R. *Anal. Chem.* **2008**, *80*, 5168–5177.
- (19) Wiseman, J. M.; Ifa, D. R.; Zhu, Y. X.; Kissinger, C. B.; Manicke, N. E.; Kissinger, P. T.; Cooks, R. G. *Proc. Natl. Acad. Sci. U.S.A.* **2008**, *105*, 18120–18125.
- (20) Nemes, P.; Vertes, A. *Anal. Chem.* **2007**, *79*, 8098–8106.
- (21) Nemes, P.; Barton, A. A.; Li, Y.; Vertes, A. *Anal. Chem.* **2008**, *80*, 4575–4582.
- (22) Apitz, I.; Vogel, A. *Appl. Phys. A: Mater. Sci. Process.* **2005**, *81*, 329–338.

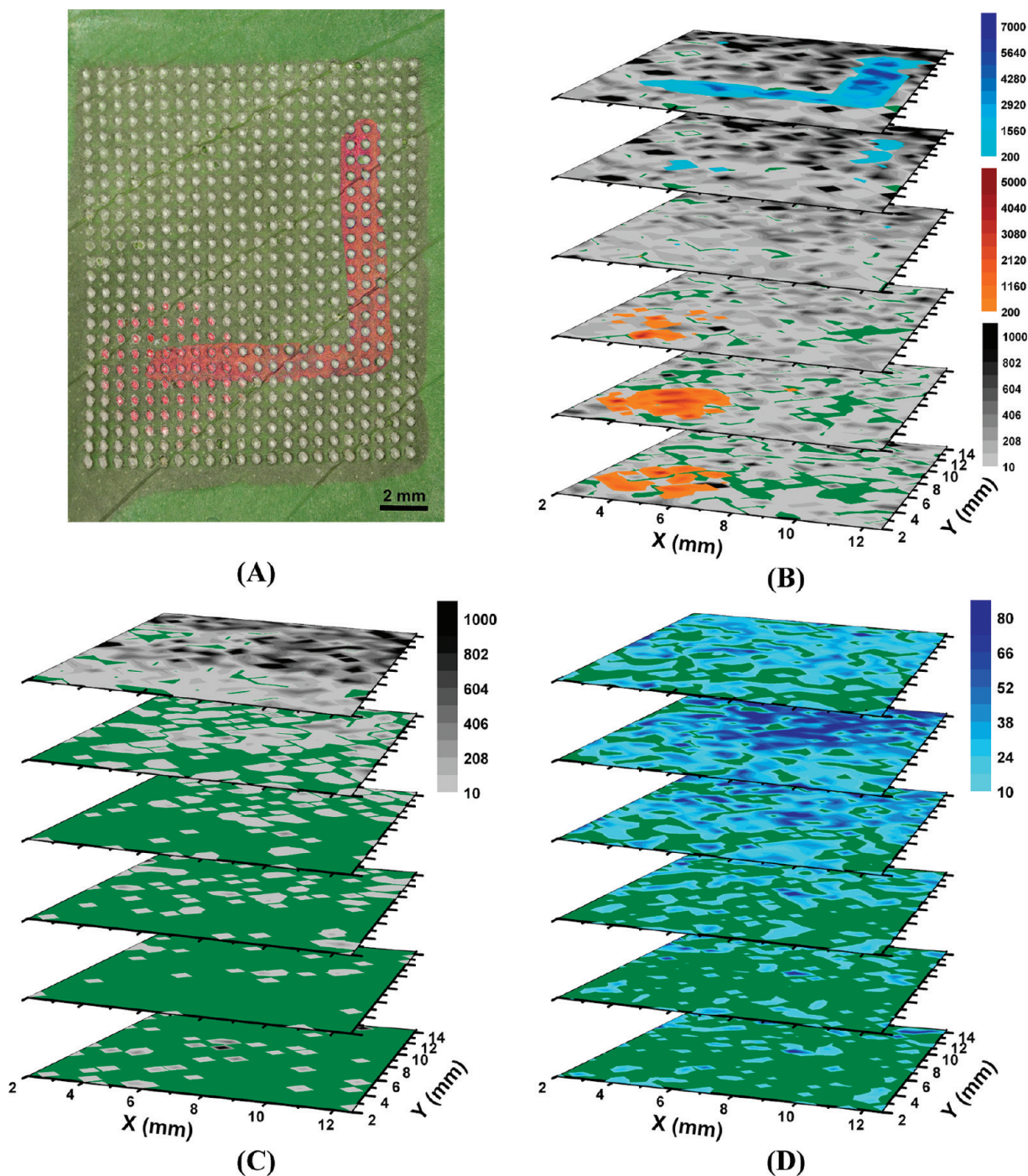


Figure 1. LAESI 3D imaging MS of *S. lynise* leaf tissue in proof-of-principle experiments. The adaxial and the abaxial cuticles were marked with right-angle lines and a spot colored in basic blue 7 and rhodamine 6G, respectively. (A) Top view of the interrogated area with an array of ablation marks. Some rhodamine 6G dye from the bottom is visible through the ablation holes. (B) Ion distributions for basic blue 7 (m/z 478.3 shown in blue color) and rhodamine 6G (m/z 443.2 shown in the orange/wine color range) on false color scales paralleled the mock patterns shown in the optical image. Higher abundances of the endogenous metabolite leucine (m/z 154.1 shown in gray color scale) were observed in the top two layers. (C) Cyanidin/kaempferol rhamnoside glucoside (m/z 595.2 shown in gray color) populated the epidermal region. (D) Chlorophyll *a* (m/z 893.5 shown in the cyan/royal blue color range) was abundant in the palisade mesophyll region, in agreement with the known localization of chloroplasts within plant tissues.

RESULTS AND DISCUSSION

Three-Dimensional Molecular Imaging by LAESI. Initially, the 3D molecular imaging capabilities of LAESI were evaluated in proof-of-principle experiments. As shown in Figure 1A, the adaxial and abaxial surfaces of an *S. lynise* leaf were marked with ~ 1 mm wide right-angle lines and a 4 mm diameter spot with basic blue 7

and rhodamine 6G dyes, respectively. Laser pulses of $2.94 \mu\text{m}$ wavelength were focused on the adaxial (upper) surface of this sample, and the laser energy was adjusted to acquire a six-step depth profile for each point on a 22×26 grid across a $10.5 \times 12.5 \text{ mm}^2$

(23) Hetherington, A. M.; Woodward, F. I. *Nature* 2003, 424, 901–908.

area. Each of the resulting 3432 cylindrical voxels with 350 μm diameter and 40 μm height, i.e., ~ 4 nL analysis volume, yielded a high-resolution mass spectrum. The top view of the leaf following LAESI 3D imaging MS can be seen in Figure 1A. A lateral step size of 500 μm yielded ~ 2 – 3 pixels to sample across the width of the lines drawn in basic blue 7. A circular rhodamine 6G dye pattern from the marking of the backside can be seen in the lower left corner of the image, indicating complete tissue removal.

The lateral and cross-sectional localization of the dye ions was followed in 3D. The color-coded contour plots in Figure 1B demonstrate the localization of the dye ions and some endogenous metabolites in the plant organ. In Figure 1B, each layer represents an ~ 40 μm thick section of the leaf tissue sampled by successive ablations. The lateral distribution of the basic blue 7 dye ion, $[\text{C}_{33}\text{H}_{40}\text{N}_3]^+$, detected at m/z 478.3260 and shown in blue in the top layer of Figure 1B was in very good correlation with its optical pattern (compare with Figure 1A). Careful inspection of the optical microscope images and the acquired spectra indicated that the laser ablation did not produce lateral mixing or cross contamination in the tissue to a significant degree. Although the basic blue 7 dye was only applied to the top cuticle of the leaf, its molecular ion was also noticed at low intensities in the second layer (< 200 counts). The corresponding pixels of the image paralleled the high-intensity areas (> 7000 counts) of the first layer, which suggested that a small fraction of the dye was transported within the tissue during the mock sample preparation step.

The molecular ion of the rhodamine 6G dye, $[\text{C}_{28}\text{H}_{31}\text{N}_2\text{O}_3]^+$, with a measured m/z 443.2295 and shown in red in Figure 1B, was found at high abundances in the fifth and six layers. Figure 1B shows that the lateral distribution patterns of the dye ion in the bottom two layers agree well with the marked spot on the abaxial cuticle seen through the ablation craters in the optical image (see Figure 1A for comparison). Plant leaves are known to have generally thinner abaxial cuticles with a higher density of stomata than the upper surface.²³ In addition to their natural role to regulate gas and water exchange with the environment, the stomata might have facilitated cross-sectional transport of the dye solution to deeper layers of the leaf during the preparation of the mock sample. Furthermore, similar to the top surface of the leaf, limited cross-sectional mixing due to laser ablation cannot be excluded.

Our cumulative experience suggests that LAESI achieves soft ionization of molecules from a variety of samples, including biological tissues that are similar in nature to those presented for analysis in this study.^{20,21,24} Similarly, when the shot-to-shot stability of ion signal for individual m/z values in LAESI ionization was tested in homogeneous samples, consecutive laser pulses showed modest fluctuation in ion intensities but no noticeable trend in the average, thus indicating the lack of laser-induced degradation (data not shown).

To further prove this point, small organics of known composition (reserpine and verapamil) were deposited on the studied leaf tissue. When LAESI spectra were collected and the background from the leaf substrate was subtracted from these spectra, stable molecular ion signal was observed with no fragmentation. These results were added to the Supporting Information. Clearly, the validity of this point also depends on the thermal stability of

the molecules of interest and the applied laser fluence. Judicious selection of the latter and critical data analysis are necessary safeguards here. For example, the ablation or postionization processes might interfere with the integrity of certain molecular classes. In particular, large noncovalent complexes might undergo dissociation in the charged droplets.

Metabolites and Their Localization. Endogenous metabolites in the leaf tissue were assigned based on their accurate masses, isotope distribution patterns, and in many cases tandem MS. The latter was especially useful in the case of the flavonoid glycosides that exhibit a wide array of structural isomers. Indeed, for these compounds not all of the structural ambiguity could be resolved. Several of the LAESI ions with a signal-to-noise ratio, S/N , > 3 were tentatively assigned to particular molecules. The tentative assignments of some observed metabolites along with the layers of their accumulation, where appropriate, are summarized in Table 1 for the leaves of both *S. lynise* and *A. squarrosa*. For the ions with the “e” superscript for the measured m/z values, tandem MS was performed. As an example, Figure 2 shows the CAD spectrum of the m/z 493 ion, tentatively assigned as, e.g., methoxykaempferol glucuronide or methoxyluteolin glucuronide. Many other positional isomers exist. The presence of the m/z 234 fragment in the CAD spectrum assigned as $^{2,4}\text{B}_0$, however, is an indication that the glucuronide is likely in the 3-O position and the structure is derived from kaempferol.²⁵ The methoxy group can still be in the 6 or the 8 position on the flavone structure. The inset in Figure 2 shows the 6-methoxykaempferol-3-glucuronide structure and its fragmentation that is consistent with the CAD spectrum.

The experiments with the mock 3D dye distributions on the *S. lynise* leaf demonstrated that LAESI allowed 3D imaging MS with low spatial resolution in the lateral and cross-sectional dimensions of the tissue, also revealing the distributions of various endogenous plant metabolites. The acquired mass spectra revealed compositional changes as a function of depth (compare mass spectra for pulses 1–6 at a particular location in Figure S1 of the Supporting Information). For example, the 3D distribution of the protonated leucine ion with m/z 154.1 can be seen in Figure 1B on a gray-to-black false color scale. This amino acid was observed across the entire tissue (with $S/N > 3$) with higher ion counts in the top 80 μm section. In contrast, the molecular ion of cyanidin/kaempferol rhamnoside glucoside with m/z 595.2 along with other secondary metabolites was uniquely linked to the top 40 μm of the tissue (shown in gray color in Figure 1C). Chlorophyll *a* with m/z 893.5 was characteristic to the palisade mesophyll layer of the leaf tissue from 40 to 80 μm (shown in the cyan/royal blue color range in Figure 1D). This result further confirmed the feasibility of LAESI 3D imaging MS in plant leaves as independent studies based on sectioning experiments had shown similar results.²⁶

Independent methods showed that a higher concentration of kaempferol glycosides is often found in the upper epidermal layers.^{26–28} In leaves of rapeseed (*Brassica napus*), for example, quercetin- and kaempferol-based UV-screening pigments are concentrated within the upper 40 μm of the leaf tissue,²⁶ showing a very good agreement with our data for *S. lynise*. Plant flavonoids are thought to play a vital role in providing protection against the

(24) Sripadi, P.; Nazarian, J.; Hathout, Y.; Hoffman, E.; Vertes, A. *Metabolomics* **2009**, *5*, 263–276.

(25) March, R. E.; Lewars, E. G.; Stadey, C. J.; Miao, X. S.; Zhao, X. M.; Metcalfe, C. D. *Int. J. Mass Spectrom.* **2006**, *248*, 61–85.

Table 1. Assignments of Selected Metabolites and Their Tissue-Specific Accumulation in *S. lynise* and *A. squarrosa*^a

metabolite	formula	monoisotopic <i>m/z</i>	measured <i>m/z</i>	Δm (mDa)	accumulation ^b
γ -aminobutyric acid ^c	C ₄ H ₉ NO ₂	104.0712 (H)	104.0701	-1.1	ADE, PM
coumarin	C ₉ H ₆ O ₂	147.0446 (H)	147.0378	-6.8	ADE
ketoglutaric acid ^c	C ₅ H ₆ O ₅	147.0293 (H)		8.5	
leucine, isoleucine ^c	C ₆ H ₁₃ NO ₂	154.0844 (Na)	154.0819	-2.5	ADE, PM
7-oxocoumarin^d	C₉H₆O₃	163.0395 (H)	163.0391	-0.4	uniform
xylose, ribose ^c	C ₅ H ₁₀ O ₅	189.0165 (K)	189.0090	-7.5	N/A
glucose ^c	C ₆ H ₁₂ O ₆	203.0532 (Na)	203.0526	-0.6	ADE
			219.0271 (K)	0.3	
ribulose phosphate ^c	C ₅ H ₁₁ O ₈ P	268.9829 (K)	268.9868	3.9	uniform
acacetin^d	C₁₆H₁₂O₅	285.0763 (H)	285.0756^e	-0.7	PM, SM, and in yellow, uni-ADE, uni-ABE
kaempferol, luteolin	C₁₅H₁₀O₆	287.0556 (H)	287.0565^e	0.9	PM, SM in yellow sectors
cyanidin^d	C₁₅H₁₁O₆	287.0556 (+)			
methylkaempferol, methyl luteolin, flavones	C₁₆H₁₂O₆	301.0712 (H)	301.0721^e	0.9	PM and in yellow
peonidin^d	C₁₆H₁₃O₆	301.0712 (+)			
methoxy-kaempferol/luteolin	C₁₆H₁₂O₇	317.0661 (H)	317.0741^e	8.0	PM, SM, and in yellow
petunidin^d	C₁₆H₁₃O₇	317.0661 (+)			
methoxy-hydroxyphenyl glucoside^d	C₁₃H₁₈O₈	325.0899 (Na)	325.0886^e	-1.3	uniform
malvidin	C ₁₇ H ₁₅ O ₇	331.0818 (+)	331.0747	-7.1	uniform
trihydroxy-dimethoxyflavone ^d	C ₁₇ H ₁₅ O ₇	331.0818 (H)			
sucrose ^c	C ₁₂ H ₂₂ O ₁₁	365.1060 (Na)	365.1058	-0.2	ADE, PM, SM
			381.0799 (K)	-0.5	
tetrahydroxy trimethoxyflavone ^d	C ₁₈ H ₁₆ O ₉	377.0873 (H)	377.0791	-8.2	PM
flavonoids ^c	C ₂₁ H ₁₈ O ₇	383.1131 (H)	383.1130	-0.1	ADE
pentahydroxy-trimethoxyflavone ^c	C ₁₈ H ₁₆ O ₁₀	393.0822 (H)	393.0839	1.7	N/A
cyanidin rhamnoside, luteolinidin glucoside ^c	C ₂₁ H ₂₁ O ₁₀	433.1135 (+)	433.1125 ^e	-1.0	ADE
kaempferol glucuronide, luteolin glucuronide ^d	C ₂₁ H ₁₈ O ₁₂	463.0877 (H)	463.0876 ^e	-0.1	PM in yellow
methoxykaempferol glucuronide^d	C₂₂H₂₀O₁₃	493.0982 (H)	493.0955^e	-2.7	PM, SM, and in yellow
kaempferide glucuronide, luteolin methylglucuronide ^c	C ₂₂ H ₂₀ O ₁₂	499.0853 (Na)	499.0936	8.3	ADE
kaempferol rhamnoside glucoside ^c	C ₂₇ H ₃₀ O ₁₅	595.1663 (H)	595.1649 ^e	-1.4	ADE
		617.1483 (Na)	617.1472	-1.1	
cyanidin rhamnoside glucoside ^c	C ₂₇ H ₃₁ O ₁₅	595.1663 (+)	595.1649 ^e	-1.4	
cyanidin diglucoside	C ₂₇ H ₃₁ O ₁₆	611.1612 (+)	611.1575	-3.7	N/A
kaempferol diglucoside ^c	C ₂₇ H ₃₀ O ₁₆	611.1612 (H)			
quercetin coumarylglucoside ^c	C ₃₀ H ₂₆ O ₁₄	633.1221 (Na)	633.1218 ^e	-0.3	N/A
kaempferol diglucuronide, luteolin diglucuronide ^d	C ₂₇ H ₂₆ O ₁₈	639.1198 (H)	639.1212 ^e	1.4	PM, SM in yellow, uni-ADE, uni-ABE
luteolin methyl ether glucuronosyl glucuronide^d	C₂₈H₂₈O₁₈	653.1354 (H)	653.1339^e	-1.5	PM, SM in yellow, uni-ADE
kaempferol-(diacetyl coumaryl rhamnoside)^d	C₃₄H₃₀O₁₄	663.1714 (H)	663.1641^e	-7.3	SM
chlorophyll a^{c,d}	C₅₅H₇₂N₄O₅Mg	893.5430 (H)	893.5425^{c,e}	-0.5^c	PM, SM^c
			893.5376^{d,e}	-5.4^d	PM, SM in green, uni-ADE, uni-ABE^d

^a Spatial cross-correlations are available for species in bold in Table 2. ^b Tissue layers are noted as adaxial epidermis (ADE), palisade mesophyll (PM), spongy mesophyll (SM), abaxial epidermis (ABE). Not available, N/A, indicates S/N < 3 for some voxels of the image. ^c Metabolites found in the leaf tissue of *S. lynise*. ^d Metabolites observed in the leaf tissue of *A. squarrosa*. ^e Tandem MS experiments facilitated metabolite assignment.

detrimental effects of solar radiation. By direct light absorption or scavenging harmful radicals these substances can create a barrier against the effect of UV-A and -B rays, protecting the photosynthetic mesophyll cells and perhaps providing them with additional visible light via fluorescence.^{28,29}

Metabolism and Tissue Architecture. We used LAESI 3D imaging MS to explore spatial variations in the metabolites of the variegated leaves of the *A. squarrosa* plant. The optical image of the adaxial side of the leaf showed alternating sectors of green and yellow color (see Figure 3A). The chemical makeup of an 11.5 × 7.5 mm² area of this tissue was probed in 3D on a 24 × 16 × 6 grid, resulting in 2304 voxels. Figure 3B presents the interrogated area, marked by an array of ablation craters. As consecutive single laser pulses sampled the composition of the tissue, mass spectra were simultaneously recorded. The detected

ions with S/N > 3 were tentatively assigned to particular molecules based on accurate mass measurements, isotope distribution analysis, and CAD experiments combined with broad plant metabolomic database searches at <http://www.arabidopsis.org>, <http://biocyc.org>, and <http://www.metabolome.jp> Web sites (last accessed on April 4, 2009).

Some of the metabolites accumulated in the mesophyll layers of the leaf tissue. In this region mass analysis showed the presence of various ions in the *m/z* 600–1000 portion of the spectrum including *m/z* 650.4, 813.5, 893.5, and 928.6. On the basis of the accurate mass (see Table 1) and the isotopic distribution pattern of the *m/z* 893.5425 ion (76% ± 4% and 50% ± 8% for M + 1 and M + 2, respectively) we assigned it as the protonated chlorophyll *a* molecule (C₅₅H₇₃N₄O₅Mg⁺ with predicted 77% and 43% for M + 1 and M + 2, respectively). CAD of the *m/z* 893.5 ion yielded an abundant fragment at *m/z* 615.2, corresponding to the protonated form of the chlorophyllide *a*, C₃₅H₃₅N₄O₅Mg⁺, as documented by other researchers.^{30–32} The 3D distribution of the chlorophyll *a* ion showed an accumulation of this species in

(26) Alenius, C. M.; Vogelmann, T. C.; Bornman, J. F. *New Phytol.* **1995**, *131*, 297–302.

(27) Strack, D.; Pieroth, M.; Scharf, H.; Sharma, V. *Planta* **1985**, *164*, 507–511.

(28) Agati, G.; Galardi, C.; Gravano, E.; Romani, A.; Tattini, M. *Photochem. Photobiol.* **2002**, *76*, 350–360.

(29) Hoque, E.; Remus, G. *Photochem. Photobiol.* **1999**, *69*, 177–192.

(30) Koichi, T.; Takakazu, K.; Masanori, M. *Anal. Sci.* **1987**, *3*, 527–530.

(31) Schoefs, B. *J. Chromatogr., A* **2004**, *1054*, 217–226.

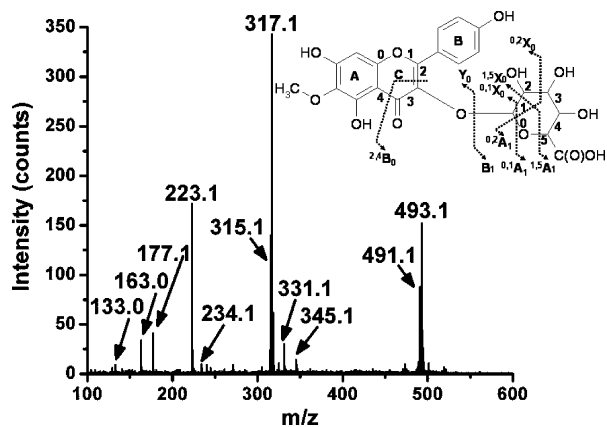


Figure 2. Tandem MS facilitated the assignment of metabolite ions in the LAESI experiments. For example, collision-activated dissociation of the m/z 493 ion yielded fragments consistent with the structure of methoxykaempferol-glucuronide. The inset shows the major fragmentation pathways proposed for 6-methoxykaempferol-3-glucuronide. The nomenclature for flavonoid glycoside fragment ions was adopted from March et al. (ref 25). The correspondence between the spectrum and the fragment ions is as follows: m/z 133.0 is interpreted as $[^{0,2}A_1 - H]^+$, m/z 163.0 is interpreted as $[^{0,1}A_1 - H]^+$, m/z 177.1 is interpreted as B_1^+ , m/z 223.1 is interpreted as $[Y_0 - C_6H_5O]^+$, m/z 234.1 is interpreted as $[^{2,4}B_0 + H]^+$, m/z 315.1 is interpreted as Y_0^+ , m/z 317.1 is interpreted as $[Y_0 + 2H]^+$, m/z 331.1 is interpreted as $[^{0,1}X_0 + 3H]^+$, and m/z 345.1 is interpreted as $[^{1,5}X_0 + H]^+$.

the second, and to some degree, in the third layers, i.e., this ion was found between 40 and 120 μm below the adaxial cuticle (see Figure 3C in blue color). Similar to our observations for *S. lysine* above, this 3D profile reflects the known biological localization of chlorophyll *a* in the chloroplasts of the palisade and spongy mesophyll layers where photosynthesis takes place.

Visual inspection of the 3D distributions provided information on the accumulation patterns of the different metabolites with respect to the morphological features of the tissue. For example, for *A. squarrosa* Figure 3C showed that kaempferol/luteolin (yellow/orange scale) exhibited heterogeneity both laterally and as a function of depth and was most abundant in the second and third layers. The blue false color scale in Figure 3C indicated that chlorophyll *a* populated the mesophyll layers. For this ion, lower intensities were observed in the yellow sectors, in agreement with their achlorophyllous nature. Figure 3D showed that acacetin, buried in layers two and three, followed the variegation pattern but did not exhibit heterogeneity in the top and bottom epidermal layers. According to Figure 3E that kaempferol-(diacetyl coumaryl)ramnoside), with m/z 663.2, accumulated in the mesophyll layers (third and fourth) with uniform lateral distributions.

Correlations between the tissue structure discerned from the optical images and the 3D molecular images of certain secondary metabolites indicated that the biosynthesis of these species was linked to the yellow sectors of the plant. For example, kaempferol/luteolin was exclusively found in the achlorophyllous tissue with higher abundances in the adaxial epidermis and the palisade and spongy mesophyll layers (see Figure 3C). These results suggested that the presence of kaempferol/luteolin was likely the result of metabolic processes active in the yellow sectors.

Figure 3D showed that the acacetin distribution was rather uniform in the first, fourth, fifth, and sixth layers. The second and third layers, however, exhibited lateral heterogeneity in the molecular distribution. The high-intensity pixels (see intensities above ~ 200 counts in red color) resembled the variegation pattern. The secondary metabolites kaempferol/luteolin diglucuronide and luteolin methyl ether glucuronosyl glucuronide exhibited similar distributions in space. These features were only partially revealed or completely obscured in our earlier 2D imaging experiments that integrated for the cross section of the tissue.²¹

The protonated ions of the methyl, methoxy, and glucuronide derivatives of kaempferol/luteolin showed similar distribution patterns (see Supporting Information, Figure S2). The optical image of the leaf cross section (data not shown) revealed that the secondary vasculature was located $\sim 150\text{--}200$ μm below the upper surface and was in direct contact with the cells of the yellow sectors. The correlation between the molecular and the optical images suggested that the glucuronide derivative localized close to the secondary veins of the leaf.

In Figure 3E, the 3D molecular image of kaempferol-(diacetyl coumaryl)ramnoside) revealed significantly higher ion counts and homogeneous presence in the spongy mesophyll (third and fourth) layers compared to the epidermal sections. For tetrahydroxy-trimethoxyflavone, the center of distribution, however, shifted toward the palisade mesophyll (second and third layers). A few ions, including those registered at m/z 501 and 647, also belonged to this group (see Supporting Information, Figures S3 and S4, respectively).

Although due to matrix and suppression effects the ion intensities often do not directly represent concentrations, relative concentration values and their correlations throughout the tissues might be evaluated. Quantitative characterization of the relationship between metabolite distributions is possible through the correlation between the normalized intensity distributions for the i th and j th ions obtained by LAESI 3D imaging MS, $I_i(\mathbf{r})$ and $I_j(\mathbf{r})$, respectively. The Pearson product-moment correlation coefficient is defined as

$$\rho_{ij} = \frac{\text{Cov}(I_i(\mathbf{r}), I_j(\mathbf{r}))}{\sigma_{I_i} \sigma_{I_j}}$$

where Cov is the covariance of the two variables in the imaged volume and σ_{I_i} and σ_{I_j} stand for the standard deviations of $I_i(\mathbf{r})$ and $I_j(\mathbf{r})$, respectively. ρ_{ij} is a measure of the connection between the distributions of the two metabolites. Spatial correlations between the intensity distributions of i th and j th ions, ρ_{ij} , can help to identify the metabolic relationship between the two chemical species.

For the metabolites in boldface in Table 1, the correlation between their 3D localization in the *A. squarrosa* leaf was evaluated through Pearson product-moment correlation coefficients. Table 2 reports the correlation coefficients calculated for the 12 selected m/z . Table S1 in the Supporting Information lists the correlation coefficients for a larger set of 26 ions.

For obvious cases, e.g., m/z 301 and 317 with $\rho_{301,317} = 0.88$, visual comparison of the distributions confirmed the strong correlation between ion distributions. The degree of similarity was also followed for less clear cases. For example, for m/z 285 and 287 with $\rho_{285,287} = 0.65$, both distributions reflected

(32) Vavilin, D.; Brune, D. C.; Vermaas, W. *Biochim. Biophys. Acta* **2005**, *1708*, 91–101.

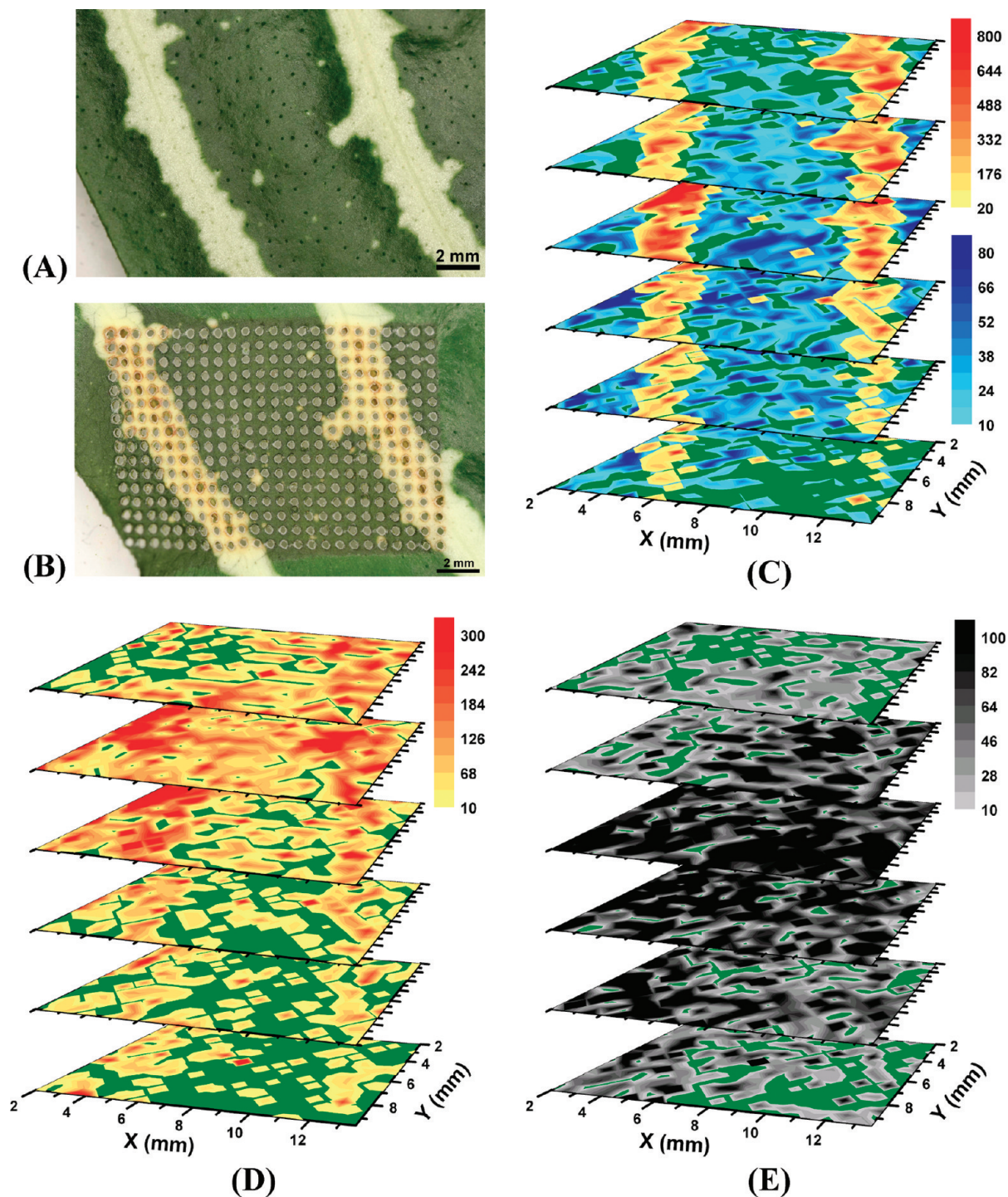


Figure 3. Metabolites in relation to tissue architecture captured by LAESI 3D imaging MS. Optical image of *A. squarrosa* leaves (A) before and (B) after analysis. (C) LAESI 3D imaging MS distribution of kaempferol/luteolin with m/z 287.0 (yellow/orange scale) followed the variegation pattern. Chlorophyll *a* with m/z 893.5 (blue scale) accumulated in the mesophyll layers. (D) Acacetin with m/z 285.0 showed higher abundance in the yellow sectors of the second and third layers with a homogeneous distribution in the others. (E) Kaempferol-(diacetyl coumaryl)rhannoside with m/z 663.2 accumulated in the mesophyll layers (third and fourth) with uniform lateral distributions.

the variegation pattern, but in layers two and three the m/z 285 distribution exhibited significant values in the green sectors, as well. Another interesting example was the lack of spatial correlation between kaempferol/luteolin at m/z 287 and chlorophyll *a* at m/z 893. The low value of the correlation coefficient, $\rho_{287,893} = 0.08$, indicated that these two metabolites were not colocalized. They are also known to belong to different metabolic pathways. Conversely, a high correlation coefficient,

$\rho_{287,301} = 0.94$, between kaempferol and methylkaempferol signified their colocalization and possibly their interconversion through the kaempferol 4'-O-methyltransferase enzyme.³³ These and other examples (see them in the Supporting Information) showed that the correlation coefficients could become a tool to uncover the connections between metabolic pathways through measuring the colocalization of metabolites in tissues.

Table 2. Pearson Product–Moment Correlation Coefficients between the 3D Spatial Distributions of Ion Intensities for 12 Selected *m/z* in an *A. squarrosa* Leaf

<i>m/z</i>	163.0 ^a	285.1 ^b	287.1 ^b	301.1 ^b	317.1 ^b	325.1 ^a	493.1 ^b	501.1 ^c	647.2 ^a	663.2 ^c	813.5	893.5 ^a
163.0	1.00	0.16	0.11	0.11	0.17	0.87	0.14	0.60	0.73	0.38	0.50	0.51
285.1		1.00	0.65	0.67	0.59	0.17	0.32	0.35	0.15	0.22	0.36	0.23
287.1			1.00	0.94	0.88	0.11	0.49	0.26	0.14	0.15	0.14	0.08
301.1				1.00	0.88	0.13	0.48	0.30	0.16	0.19	0.18	0.10
317.1					1.00	0.19	0.64	0.35	0.22	0.21	0.18	0.14
325.1						1.00	0.17	0.73	0.87	0.49	0.20	0.61
493.1							1.00	0.32	0.20	0.16	0.16	0.16
501.1								1.00	0.83	0.83	0.71	0.61
647.2									1.00	0.71	0.57	0.55
663.2										1.00	0.51	0.43
813.5											1.00	0.65
893.5												1.00

^a See Figure S4 of the Supporting Information for the related distributions. ^b See Figure S2 of the Supporting Information for the related distributions. ^c See Figure S3 of the Supporting Information for the related distributions.

CONCLUSIONS

This work reports the first example of 3D imaging MS at atmospheric pressure and provides a method to correlate molecular composition with tissue morphology. This novel development was a nontrivial combination of lateral imaging and molecular depth profiling capabilities that had been independently presented in a previous publication.²¹ Successful 3D imaging put dramatically higher stability requirements on the LAESI ion source. Data acquisition protocols and data reduction and analysis were also more complex. Finally, the amount and quality of information gathered in a 3D experiment is significantly higher. This is most obvious in the case of the established spatial correlations of ion abundances.

LAESI 3D imaging MS revealed the distribution of secondary metabolites in correlation with tissue specificity in plants.³⁴ We anticipate that with LAESI eventually water-containing organs or whole-body sections of plants and animals, as well as human tissues, can be analyzed in 3D under ambient conditions for multiple chemical species.

In principle, working at atmospheric pressure also enables the study of live specimens. Although locally destructive, laser ablation of small, e.g., 300 μm diameter, areas of a larger plant or animal can leave the entire organism viable. Even the ablated cells are alive and nonmodified up to the moment of analysis, occurring on the millisecond time scale, so their chemical composition can reflect their condition and functioning at the time of the ablation.

Although 3D ambient imaging with LAESI has been proven feasible in plant tissues, further improvements are needed in spatial resolution. For example, major variations in the water content or tensile strength of tissues can affect the lateral imaging and depth profiling performance of the method. If these properties change in the tissue, a preselected laser fluence might result in variations in the ablation depth. An automated feedback mechanism could correct for these effects by recording the depth of ablation for each laser pulse and adjusting the laser energy and/or wavelength to minimize depth variations. With the current lateral and depth resolutions of ~ 300 and ~ 30 μm , respectively, LAESI offers low spatial resolving power in comparison to optical and established vacuum MS imaging techniques. Reduced spot

sizes are expected from a focusing system with low spherical aberration or from coupling the laser energy into the sample through a sharpened optical fiber. These two approaches promise the metabolic analysis of single cells with dimensions down to ~ 10 μm , while maintaining good signal-to-noise ratios in the mass spectra. LAESI imaging with these improved lateral and depth resolutions can enhance our understanding of the spatial organization of tissues as well as cell-to-cell communication and molecular transport.

Instantaneous information on the chemistry of biological and medical specimens without sample treatment can be useful in a variety of applications. Diverse applications in plant biology, in pharmacokinetic studies of absorption, distribution, metabolism, and excretion (ADME) of drugs, endogenous metabolites, and xenobiotics are also expected to benefit from LAESI 3D imaging MS.

ACKNOWLEDGMENT

The authors are grateful for the financial support of this work by the U.S. National Science Foundation under Grant No. 0719232, by the U.S. Department of Energy (DEFG02-01ER15129), and by the W. M. Keck Foundation (041904).

SUPPORTING INFORMATION AVAILABLE

Animated GIF image of the microscope investigation of the *S. lynise* tissue following LAESI sampling with a single laser pulse delivered on the adaxial (upper) epidermis; differential interference contrast microscope images captured in the *Z*-stack mode for a series of focal planes with a 5 μm depth step to optically map the resulting ablation crater; these depth-resolved images were then combined into a GIF animation; the ablation depth was determined to be ~ 35 μm ; an example for a broad Pearson product–momentum cross-correlation analysis for the 3D molecular distributions of 26 ions (Table S1); mass spectra that demonstrate varying molecular composition as the leaf tissue of *S. lynise* is ablated by six consecutive laser pulses (Figure S1); groups of metabolites with similar 3D distribution patterns in the leaf of *A. squarrosa* (Figures S2–S4). This material is available free of charge via the Internet at <http://pubs.acs.org>.

Received for review April 7, 2009. Accepted June 10, 2009.

AC900745E

(33) Schroder, G.; Wehinger, E.; Lukacin, R.; Wellmann, F.; Seefelder, W.; Schwab, W.; Schroder, J. *Phytochemistry* **2004**, *65*, 1085–1094.

(34) DellaPenna, D.; Last, R. L. *Science* **2008**, *320*, 479–481.